

Article

# Determination of Region of Influence Obtained by Aircraft Vertical Profiles Using the Density of Trajectories from the HYSPLIT Model

Henrique L.G. Cassol <sup>1,\*†</sup>, Lucas G. Domingues <sup>2,3,\*†</sup>, Alber H. Sanchez <sup>3</sup>, Luana S. Basso <sup>3</sup>, Luciano Marani <sup>3</sup>, Graciela P. Tejada <sup>3</sup>, Egidio Arai <sup>1</sup>, Caio Correia <sup>3,4</sup>, Caroline B. Alden <sup>5</sup>, John B. Miller <sup>6</sup>, Manuel Gloor <sup>7</sup>, Liana O. Anderson <sup>8</sup>, Luiz E. O. C. Aragão <sup>1</sup> and Luciana V. Gatti <sup>3,4,\*</sup>

<sup>1</sup> Remote Sensing Division, National Institute for Space Research (INPE), Av. dos Astronautas, 1758, São José dos Campos 12.227-010, Brazil; egidio.arai@inpe.br (E.A.); laragao@dsr.inpe.br (L.E.O.C.A.)

<sup>2</sup> National Isotope Centre, GNS Science, Lower Hutt 5010, New Zealand

<sup>3</sup> Earth System Science Center (CCST), National Institute for Space Research (INPE), Av. dos Astronautas, 1758, São José dos Campos 12.227-010, Brazil; alber.ipia@inpe.br (A.H.S.); luanabasso@gmail.com (L.S.B.); lmarani@gmail.com (L.M.); gracielaatejadap@gmail.com (G.P.T.); cacorreia@gmail.com (C.C.)

<sup>4</sup> Nuclear and Energy Research Institute (IPEN), Avenida Lineu Prestes, 2242, São Paulo 05508-000, Brazil

<sup>5</sup> CIRES, University of Colorado Boulder, 216 UCB, Boulder, CO 80309, USA; aldenc@colorado.edu

<sup>6</sup> NOAA Global Monitoring Laboratory, Boulder, CO 80305, USA; john.b.miller@noaa.gov

<sup>7</sup> School of Geography, University of Leeds, Leeds LS92JT, UK; eugloor@gmail.com

<sup>8</sup> National Center for Monitoring and Early Warning of Natural Disasters—Cemaden, Estrada Doutor Altino Bondesan, 500—Distrito de Eugênio de Melo, São José dos Campos 12.247-016, Brazil; liana.anderson@cemaden.gov.br

\* Correspondence: henrique.cassol@inpe.br (H.L.G.C.); l.domingues@gns.cri.nz (L.G.D.); Luciana.gatti@inpe.br (L.V.G.); Tel.: +55-12-3208-6465 (H.L.G.C.)

† These authors contributed equally to this work.

Received: 15 September 2020; Accepted: 30 September 2020; Published: 9 October 2020

**Abstract:** Aircraft atmospheric profiling is a valuable technique for determining greenhouse gas fluxes at regional scales ( $10^4$ – $10^6$  km<sup>2</sup>). Here, we describe a new, simple method for estimating the surface influence of air samples that uses backward trajectories based on the Lagrangian model Hybrid Single-Particle Lagrangian Integrated Trajectory Model (HYSPLIT). We determined “regions of influence” on a quarterly basis between 2010 and 2018 for four aircraft vertical profile sites: SAN and ALF in the eastern Amazon, and RBA and TAB or TEF in the western Amazon. We evaluated regions of influence in terms of their relative sensitivity to areas inside and outside the Amazon and their total area inside the Amazon. Regions of influence varied by quarter and less so by year. In the first and fourth quarters, the contribution of the region of influence inside the Amazon was 83–93% for all sites, while in the second and third quarters, it was 57–75%. The interquarter differences are more evident in the eastern than in the western Amazon. Our analysis indicates that atmospheric profiles from the western sites are sensitive to 42–52.2% of the Amazon. In contrast, eastern Amazon sites are sensitive to only 10.9–25.3%. These results may help to spatially resolve the response of greenhouse gas emissions to climate variability over Amazon.

**Keywords:** footprint; transport pathway; carbon dioxide; greenhouse gases; atmospheric aircraft profiles

## 1. Introduction

Greenhouse gas (GHG) fluxes occur at various spatial scales, from the molecular level to global cycling, meaning that analysis strongly depends on the spatial scale. The level of complexity of these GHG fluxes changes during upscaling analysis as a function of the interrelations among physical, chemical, and biological processes [1,2]. The method for upscaling leaf- to landscape-scale terrestrial flux processes is known as the bottom-up approach. In this approach, on-the-ground data may be combined and constrained to estimate GHG fluxes from the surface using process- or empirical-based vegetation models [3]. For example, in the carbon cycle, process-based models simulate the underlying biogeochemical mechanisms (e.g., respiration, photosynthesis, and fire emissions) to constrain carbon flux for each plant functional type [3]. On the other hand, top-down approaches include the mass balance method, transport inversion, and atmospheric models with ground, tower, aircraft, and satellite observations to estimate surface fluxes by minimizing the differences between simulated and observed atmospheric GHG mole fraction measurements [4,5] (Figure 1).

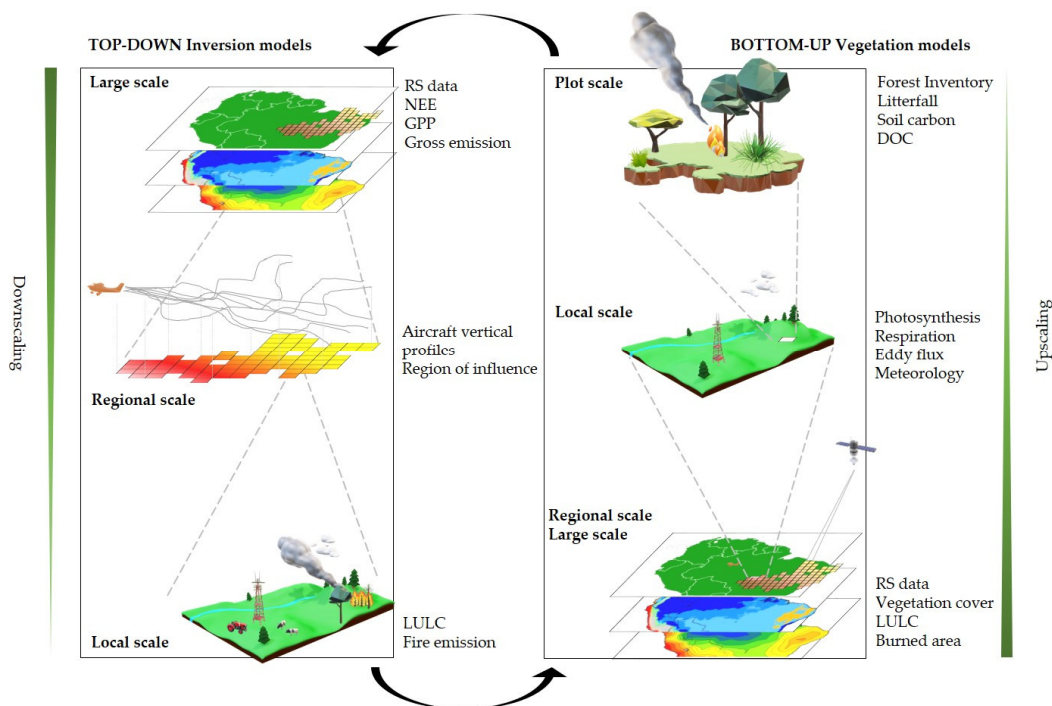


**Figure 1.** Overview of bottom-up and top-down approaches. Aircraft observational data are representative of an intermediate (regional) spatial scale and can be used to estimate regional fluxes. These regional fluxes can be used for both validations of upscaling of local fluxes and as a starting point for flux downscaling.

Atmospheric measurements can constrain fluxes of CO<sub>2</sub> and other GHGs at a variety of scales. At relatively small scales, eddy covariance observations constrain net fluxes of CO<sub>2</sub> through high-frequency (>1 Hz) measurements made at a local scale measurement tower [6,7]. The region of influence of the tower covers an area of approximately 1 km<sup>2</sup> and depends mainly on the type of forest and tower height, and the eddy covariance data can provide insights on biophysical variables controlling exchanges [8]. At much larger scales, highly calibrated CO<sub>2</sub> mole fraction measurements, largely from remote global locations, can constrain terrestrial CO<sub>2</sub> fluxes primarily at continental scales [9,10]. Between the resolution and spatial coverage of eddy covariance measurements and most global inverse models, there is a large missing scale. These regional scales, which we define to be of the order of 10<sup>4</sup>–10<sup>6</sup> km<sup>2</sup>, are important scales over which to determine GHG fluxes because they often relate to scales of climate anomalies and ecosystem variation that can influence GHG fluxes. Thus,

improved understanding of GHG fluxes at regional scales can improve our understanding of the processes controlling them.

Regional-scale fluxes can be determined using bottom-up approaches by upscaling the eddy covariance measurements of the Net Ecosystem Exchange (NEE) using meteorological and remote sensing data, such as those used in the FLUXCOM [11]. As mentioned earlier, another bottom-up approach is the use of process-based terrestrial biosphere models to determine GHG fluxes within a given area. These bottom-up approaches have the potential for presenting considerable uncertainties relating to imperfect parameterizations of complex ecophysiological processes (in the case of models) and errors in meteorological and remote sensing data sets. An alternative approach to determining regional-scale GHG fluxes is the use of well-calibrated GHG mole fraction measurements made on air samples collected from aircraft vertical profiles extending from the surface to the lower/middle troposphere [5,12,13]. Top-down, regional-scale fluxes determined from such profiles are sensitive to all upstream fluxes, known and unknown. This represents an advantage over bottom-up estimates, which may not account for all processes, although top-down fluxes generally do not provide much spatial resolution and instead constrain the spatial integral of fluxes. Top-down fluxes are also uncertain as a result of assumptions or parameterization about atmospheric flow and mixing. Despite some drawbacks of regional-scale top-down fluxes, they can complement the information contained within high-resolution bottom-up approaches and the information obtained from large-scale inverse model studies.

Regional fluxes based on vertical profiles may provide additional information in understanding differences between GHG fluxes estimated from bottom-up approaches and large-scale inverse models. Conflicting results of estimated CO<sub>2</sub> sinks and sources have been observed between bottom-up approaches and inversion models in the tropics. Recently, Kondo et al. [14] pointed out a significant C sink from Support Vector Regression (SVR) from eddy covariance FLUXNET sites (bottom-up) in the tropics. In contrast, neutral CO<sub>2</sub> fluxes were observed in an intercomparison among several inversion models (top-down) [14]. In this example from Kondo et al. [14], it is unclear whether the discrepancy in tropical flux arises from issues in eddy covariance NEE upscaling or possibly from seasonal gaps in the tropical coverage of the Greenhouse gases Observing SATellite (GOSAT) CO<sub>2</sub> due to seasonal cloudiness [15]. Regionally representative vertical profiles, if available, would help to constrain the fluxes better.

The “regions of influence” associated with vertical profiles that are described and analyzed in this study need to be distinguished from “footprints” which are described by Lin et al. [16] and Stohl et al. [17] both in their construction and use. Although both regions of influence and footprints are derived from back-trajectory models forced by meteorological input (mainly horizontal wind fields), there are some important differences. Footprints quantify the sensitivity of mole fraction at an observation point (often referred to as the “receptor”) to upwind fluxes of a gas. Footprints are determined from an ensemble of randomly perturbed back-trajectories released at each measurement point. In contrast, and as described in detail below, our regions of influence are calculated from single back-trajectories released from each measurement point. Binning trajectories create the ensemble of trajectories used to define the region of influence over most of the depth of the profile over three months. Footprints are also typically used as sensitivity matrices in Bayesian estimates of GHG fluxes in inversions, where the footprints project fluxes into mole fraction deviations (and vice versa) [18,19]. In contrast, the regions of influence described here are not intended to be used to calculate GHG fluxes from atmospheric data. Regions of influence can instead be used to (a) combine and compare GHG flux estimates from areas upwind of different sites and (b) determine the average value of meteorological variables such as temperature and precipitation in the area upwind of a site.

The estimation of regional fluxes based on GHG mole fractions from aircraft vertical profile air samples [5,12,13] can help constrain and thus improve our understanding of natural and anthropogenic GHG fluxes differences between bottom-up and top-down estimates. Regional flux observations can also improve biosphere model performance such that source and sink processes can be more accurately parameterized [14] to support policymakers in their efforts to regulate carbon emissions [20].

The goal of our research is to describe a method to compute the region of influence for atmospheric aircraft vertical profiles observations using back-trajectories of the HYSPLIT model [21]. We analyzed regions of influence for four vertical profiling sites in the Amazon Basin on a quarterly basis, over nine years. In addition, we addressed two questions for each site: (a) how large are the regions of influence inside and outside the Amazon (in km<sup>2</sup>)? (b) what is the relative area of the regions of influence inside the Amazon (in %)?

## 2. Experiments

### 2.1. Amazon Mask

We are considering the Amazon subregions of Amazonia sensu stricto, Andes, Guiana, and Gurupí that have most of the Tropical and subtropical moist broadleaf forest, and we exclude the Planalto region because it has predominantly tropical and subtropical grasslands, savannas, and shrublands (Figure 2) [22,23]. The Amazon mask was defined by the CARBAM project (the Amazon carbon balance long-term study [24], with an area of 7,256,362 km<sup>2</sup> (Figure 2a), and based on the Amazon boundaries of Eva et al. [22] and the biomes of Olson et al. [23]. Although Amazon has no defined limits considering air masses, we opt to select this boundary to compute the contribution of the region of influence inside and outside the mask.

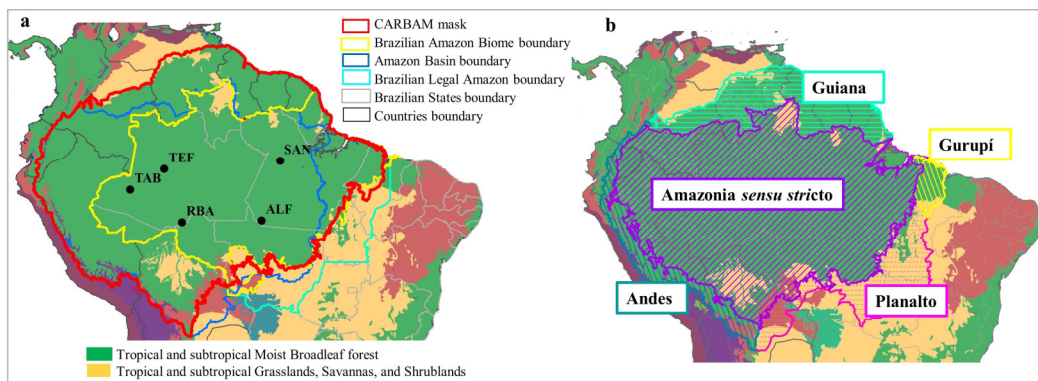


**Figure 2.** (a) CARBAM mask (Amazon study area) and flight collection sites: ALF, SAN, RBA, TAB, and TEF are represented by black circles. South American biomes are from Olson et al. [23]; (b) Amazon subregions used to define the CARBAM mask (with the Planalto exception) of Eva et al. [22].

### Description of CARBAM Flight Collection Sites

The four CARBAM sampling sites are spread across Amazonia: one southwestern site (RBA—9.38° S, 67.6° W), one northwestern site (TAB—5.96° S, 70.1° W between 2010 and 2012, replaced by TEF—3.31° S, 65.8° W since 2013), one northeastern site (SAN—2.86° S, 54.9° W), and one southeastern site (ALF—8.80° S, 56.7° W). According to Gatti et al. [25], the SAN site is not only influenced by tropical forest, but also by nonforest biomes, mainly the Cerrado (savanna) and the Caatinga, and the major city—Belem (2.5 million people) in Para state. The ALF site is also on the eastern side and has a limit of Cerrado (Planalto region in Figure 2b).

Amazon rainfall varies spatially with relatively low variability throughout the year in the northwestern basin that receives more than 2800 mm/y, while precipitation in the southeastern basin is strongly seasonal, with peak rainfall occurring in January and a long dry season centered on July with an annual total amount of around 1600 mm/y. The south and southeastern portions of the basin have a lower mean annual precipitation and more extended dry season (4–5 months with <100 mm rainfall) [26].

TAB has no dry season (defined as any month with less than 100 mm of rainfall), while TEF has a two-month dry season, with the lowest rainfall in August and climate classification of “Af”—tropical forest climate. RBA has a dry season length of three months (JJA), with a peak in July and a

climate classification of “Am” —tropical monsoon climate. ALF has a four-month dry season (JJAS), with a peak in July, climate “Aw” —tropical savanna climate; SAN has a five-month dry season (JASON), with the lowest rainfall in August and a climate classification “Am” [27].

The northwest region, where TAB and TEF are located, is the most preserved region among the four aircraft vertical profiles sampling sites. ALF and south of RBA are in the “Arc of Deforestation” where land use and cover change predominate, mostly with agriculture and grasslands in Brazil and Bolivia [28–31].

## 2.2. Aircraft Vertical Profile Air Sampling

The vertical profile air sampling program started in 2000 with a single site at SAN [25,32] and expanded to the four sites from January 2010 [12]. The sampling profile collection was performed mainly two times per month over the same geographical position at each site, totaling around 600 vertical profiles between 2010 and 2018. The sampling flights were performed using small aircraft between 12:00 and 13:00 local time in a descending spiral profile to avoid the aircraft emission. This time is preferred because the planetary boundary layer is more fully developed [20].

A vertical profile is typically composed of 12 to 17 air samples collected at altitudes varying from 300 m to 4420 m asl using small aircraft equipped with a semiautomatic sampling system developed by the National Oceanic Atmospheric Administration Global Monitoring Laboratory (NOAA/GML) [25]. This system consists of two units: the Programmable Compressor Package (PCP), which pressurizes ambient air into glass flasks held in the second unit, the Programmable Flask Package (PFP). Each flask is filled by remote control by the pilot at a preprogrammed altitude; the sampling altitudes from each site are shown in Table S1.

The sampling system also has a temperature, pressure, and humidity sensor, and a GPS. Figure 3 shows the three airplane models used to carry out GHG sampling in the scope of the CARBAM project, detailing the sample inlet and the PFP and PCP suitcases.



**Figure 3.** Airplanes used to collect greenhouse gases in the sites. Red arrows highlight the collector tube and the Programmable Flask Package (PFP) and Programmable Compressor Package (PCP) suitcases, respectively. (A). Model Seneca for RBA site and TAB site sampling, (B). Model Sertanejo for SAN site sampling. (C). Model Cessna 210 for ALF site sampling. Source: Domingues [33], with permission.

For each site, we calculated influence functions for two vertical profiles per month, filling vertical profile gaps simulating flights using the same input parameters, such as altitude, site, and hour to be used in the HYSPLIT model (Table 1). Study areas have gaps in scheduled flights either due to logistical problems (mostly rain) or the discontinuity of the project in the 2015–2016 period.

**Table 1.** Number of scheduled flights over study areas. Study sites: TAB/TEF, RBA, SAN, and ALF.

Year	Number of Flights (Number of Simulated Flights)			
	TAB/TEF	RBA	SAN	ALF
2010	19(5)	19(5)	19(5)	19(5)
2011	14(10)	17(7)	22(2)	18(6)
2012	9(15)	22(2)	24(0)	24(0)

2013	8(16)	17(7)	23(1)	21(3)
2014	16(8)	13(12)	16(8)	17(7)
2015	4(20)	11(14)	6(18)	5(19)
2016	0(24)	20(4)	0(24)	20(4)
2017	14(10)	21(3)	17(7)	24(0)
2018	13(11)	20(4)	18(6)	24(0)
<b>Total</b>	97(119)	160(56)	145(71)	172(44)

### 2.3. The HYSPLIT Model

Our back-trajectories are simulated using the Hybrid Single-Particle Lagrangian Integrated Trajectory Model (HYSPLIT, NOAA-ARL) downloaded package version 4, with meteorological input data from the Global Data Assimilation System (GDAS,  $1^\circ \times 1^\circ$ , 3 h. resolution) [21,34]. HYSPLIT is one of the most extensively used atmospheric transport and dispersion models in the atmospheric sciences community. Many research studies have used HYSPLIT trajectories to determine possible source regions of contributing measurements of selected pollutants or to determine air masses that may have affected a location under study [34,35]. For example, the HYSPLIT model was recently used to calculate the backward trajectory and geographic data analysis for the ATTO site in the central Amazon Basin [36]. In addition, this model is used operationally by NOAA and other federal agencies to run complex atmospheric transport simulations [37].

The model calculation method is a hybrid between the Lagrangian approach, which uses a moving frame of reference for the advection and diffusion calculations as the trajectories or air parcels move from their initial location, and the Eulerian method, which uses a fixed three-dimensional grid as a frame of reference to compute pollutant air mole fractions [34]. In HYSPLIT, there is no convective parametrization; the mixing of the particles occurs in the vertical motion field from meteorological data input [34].

Back-trajectories start from the day, time, and altitude of the collection point (in m asl) from the central point of each overflight geographic location as stated in Figure 2, and spatially locate points every hour for 13 days prior to the collection time (Figure 4), for all flights performed over the study sites. The latitude and longitude of each back-trajectory for a vertical profile are the same because the vertical profile, to within a few km, is centered above a single point on the surface. Each trajectory has approximately 312 location points (13 d  $\times$  24 h) with the position of the air masses (latitude, longitude, and altitude) relative to their origin at every hour (Figure 4), which results in between 12 and 17 individual back-trajectories per flight, stored as ASCII files. Despite collecting air samples up to 4420 m, the regions of influence are based only on back-trajectories between 300 and 3500 m asl because trajectories either starting or traveling through this altitude range are the ones most likely to be sensitive to surface fluxes. Up to 3500 m asl, surface fluxes mix into the planetary boundary layer (PBL), which is typically around 1300 m asl, and some mixing occurs above these altitudes due to processes including dry and moist convection and plume rise associated with biomass burning. The cutoff level of 3500 m is supported by two observations: first, biomass burning plumes rarely exceed 3500 m asl (Figure S1); and second, mole fractions of CO<sub>2</sub> and other gases observed above 3500 m asl are very similar to gas mole fractions from measurements in the Tropical Atlantic marine boundary layer, which indicates minimal Amazonian surface influence [13]. Additionally, as we report in the discussion below, changing the upper altitude limit from 3500 to 1300 m has a minimal impact on our results.

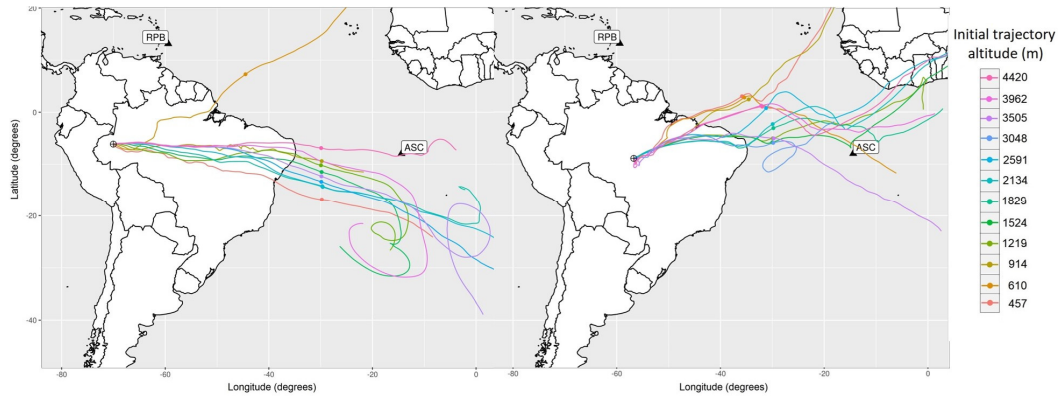


**Figure 4.** Example of the back-trajectories at each initial altitude of collection, whereby each colored line represents the collection flask by overflight altitude. Back-trajectories at the ALF site for 17 February 2010 (**left**) and at the TAB site for 20 April 2011 (**right**). The point on the trajectories represents the crossing point between two segments of a virtual limit, the first one is a latitude limit, from the equator southwards at 30° W, and the second segment is a line between NOAA stations (Barbados—RPB; Ascension—ASC; and Cape Point—CPT). This virtual limit is used to estimate GHG background concentrations for Amazon sites (see details at Domingues [38]).

#### 2.4. Region of Influence

By definition, we consider the region of influence to be those areas covered by the set of back-trajectories by each profile and altitude integrated over a period. Back-trajectory models such as HYSPLIT can have high uncertainties in predicting where particles are coming from accurately [16,17], as we can note in Figure 4 with a spurious air trajectory at 900 m at the TAB site coming from the Northern Hemisphere. This deviation is due to several parametrizations for vertical and horizontal mixing in the atmosphere, including a convective boundary layer, circulation models, height integration models, and air temperature, humidity, and pressure [16]. Therefore, a reasonable method to reduce the impact of such uncertainties, as well as smaller random errors, is to consider an ensemble of back-trajectories over a period (like three months or a year). We noted several differences between the approach presented here and the estimation of regions of influence previously used by Gatti et al. [12]. In the case of Gatti et al. [12], the region of influence was determined from the northernmost and southernmost trajectory boundaries for a given site (over a two-year period), and weighting within that region was not considered. In contrast, here, regions of influence are calculated on a quarterly basis and also contain spatial information on the relative influence of the surface with each region of influence. Finally, in the present study, calculation of back-trajectories was performed using meteorology with a resolution of  $0.5^\circ \times 0.5^\circ$  instead of  $1^\circ \times 1^\circ$ .

The trajectory density,  $d_i$ , is determined as the sum of the number of back-trajectory points (at a one-hour frequency) within each one-degree cell. We binned the trajectories into quarters instead of years in order to understand the seasonal patterns of atmospheric circulation influencing air samples collected at each site. The density of trajectories was calculated by grouping the back-trajectories in the first quarter, second quarter, and so on by year and site. All these processing steps were performed in the R software environment for statistical computing and graphics [39].

Using IDL® programming (IDL; ITTVis Inc.), the South American map of trajectory densities was positioned in a global one-degree grid ( $360^\circ \times 180^\circ$ ) and land grid cells were identified (and ocean grid cells not considered) using a South America grid of  $1^\circ \times 1^\circ$  resolution. The weighted density of trajectories ( $w_i$ ) at each grid cell ( $i$ ) is given by the ratio of trajectory densities in each land grid cell ( $d_i$ ) to the sum of all trajectory points over South America as:

$$w_i = \frac{d_i}{\sum_{i=1}^k d_i} \quad (1)$$

where  $k$  is the number of land grid cells in South America. Maps of  $w$  are the “regions of influence” and are computed for each of 36 quarters (9 years  $\times$  4 quarters) at each of the four sites. Figure 5 shows mean quarterly regions of influence for each site.

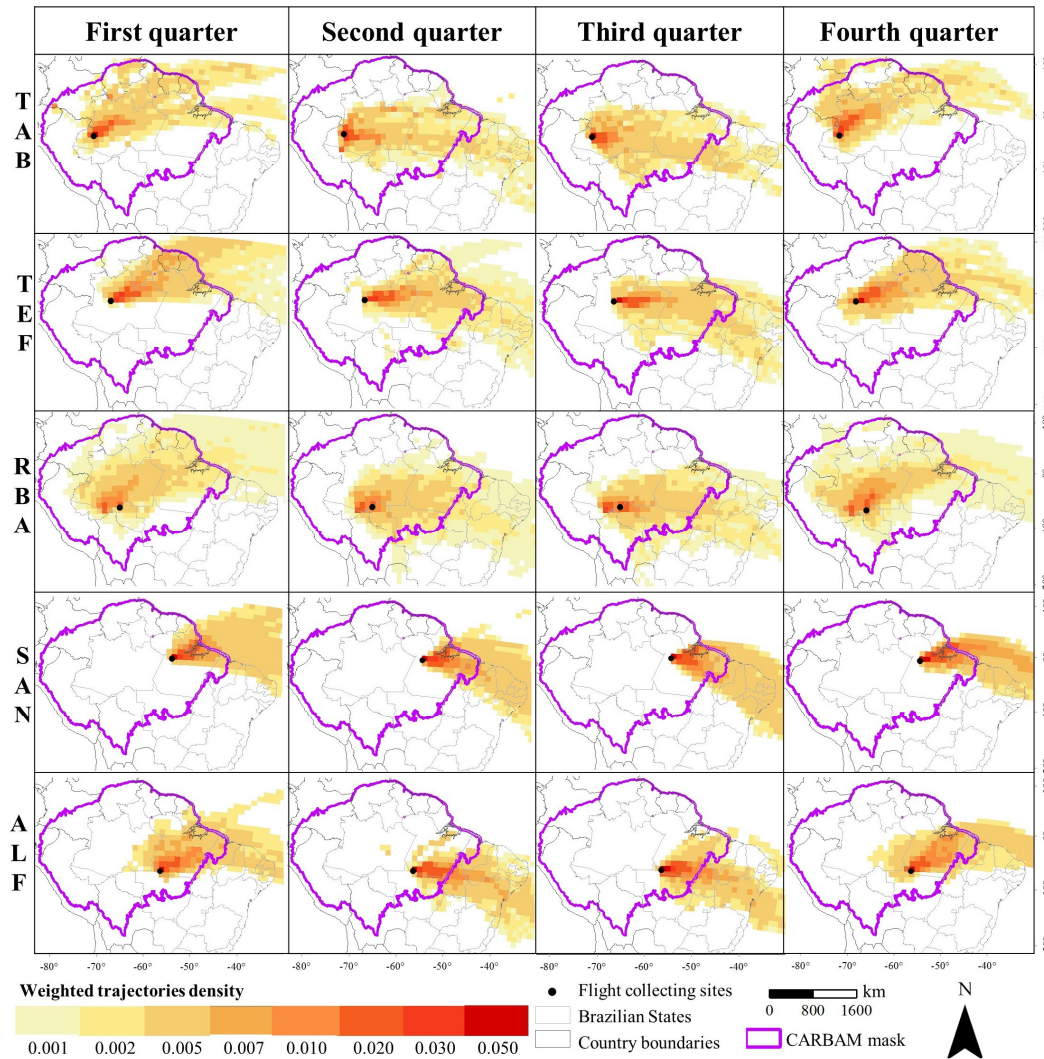


**Figure 5.** Quarterly regions of influence (maps of  $w$ , calculated according to Equation (2)) averaged between 2010 and 2018 for all vertical profiling sites, except that TAB was in existence only between 2010 and 2012 and TEF existed between 2012 + 1 and 2018. Warmer colors represent the highest densities of trajectories in the  $1^\circ \times 1^\circ$  resolution cell in the CARBAM sites: ALF, SAN, RBA, and TAB/TEF. Months of the quarters are: First Quarter—January, February, and March; Second Quarter—April, May, and June; Third Quarter—July, August, and September; Fourth Quarter—October, November, and December.

The percentage of the weighted points of trajectories within the Amazon, “ $Amz\_perc$ ”, is given by the ratio of the sum of the weighted density of trajectories ( $w_i$ ) placed inside the Amazon grid cells,  $w_i(AMZ)$  to the sum of  $w_i$  inside the South America  $w_i(SA)$  by quarter, site and year, as (2):

$$Amz\_perc(\%) = \frac{\sum_{i=1}^l w_i(AMZ)}{\sum_{i=1}^k w_i(SA)} 100 \tag{2}$$

where  $l$  is the number of  $1 \times 1$  grid cells inside the Amazon CARBAM mask (Figure 2). One value of  $Amz\_perc$  is calculated for each quarter at each site. The region of influence outside the Amazon is defined by  $100 - Amz\_perc(\%)$ .

### The Relative Area inside Amazon

We also calculated the unweighted relative area,  $rel_{area(\%)}$ , for each region of influence in the Amazon CARBAM mask, given by the ratio of the sum of grid cells with at least one trajectory point inside the Amazon and the sum of grid cells with at least one trajectory point outside Amazon, defined as the relative area (3):

$$rel_{area(\%)} = \frac{\sum_{i=1}^l \Omega_i (AMZ)}{\sum_{i=1}^k \Omega_i (SA)} 100 \quad (3)$$

where  $(\Omega_i)$  has a value of 1 if there is at least one trajectory point in the grid cell; otherwise, it is 0.

Finally, the “weighted area” inside the Amazon is given by the product of the fractional weighted density of trajectories ( $Amz\_perc$  as a fraction) and the sum of the pixel area divided by the area of the Amazon CARBAM mask (7,256,362 km<sup>2</sup>) (4):

$$weighted_{area} = \frac{\sum_{i=1}^l Wi(AMZ)}{\sum_{i=1}^k Wi(SA)} \sum_{i=1}^N \left( \frac{Apixel\_i}{AreaAmz} \right) \quad (4)$$

where  $weighted_{area}$  is the weighted area inside the Amazon considering the region of influence and its relative area.  $N$  is the number of pixels in the Amazon with at least one trajectory crossing for each quarter, site, and year.  $Apixel$  is the area of a one-degree pixel in km<sup>2</sup> (approximately  $111 \times 111$  km<sup>2</sup> near the equator), and  $AreaAmz$  is the area of the Amazon mask. The unweighted area is given by the sum of pixel areas in the region of influence with at least one density trajectory point, i.e.,  $unweighted_{area} = \sum_{i=1}^N (Apixel\_i)$ .

## 3. Results

### 3.1. Quarterly Patterns of the Regions of Influence

The regions of influence follow the pattern of atmospheric circulation at each study site. Figure 5 shows the average of the region of influence by quarters given by the density of trajectories through the 2010–2018 period. The highest density of trajectories is found nearby the place where the atmospheric vertical profiles are collected (reddish cells) and spread around it, generally towards the northeast (yellowish cells).

From Figure 5, we can highlight that regions of influence are seasonally variable at the vertical profiling sites. The first and fourth quarters (generally, the rainy season) have a well-defined behavior in the eastern Amazon, whose trajectories, in some parts, originate in the Northern Hemisphere to the northeast. In the second and third quarters (dry period), the air masses that enter the continent are from the Southern Hemisphere exclusively.

Typical circulation in the Amazon involves the air masses coming from the Atlantic Ocean along the northeast coast, crossing the Amazon, and heading towards the Andes. During the periods from October to December (fourth quarter) and January to March (first quarter), the Intertropical Convergence Zone (ITCZ) is south of the equator bringing air masses from the Northern Hemisphere, shaping the region of influence northward (Figure 5). For the remainder of the year, the ITCZ returns to the north of the equator and air masses come from the Southern Hemisphere, exclusively [40].

The ITCZ oscillation has direct importance on annual climatological and hydroclimatological variability across the Amazon where the predominant air masses direction varies from the north to the south and from the east to the west. Understanding variations on regional patterns of atmospheric circulation is a critical step to provide knowledge on the origins of the GHG fluxes. As shown in Marengo et al. [41], rainfall in the southern Amazon peaks in January–February (ALF and RBA) during the austral summer, while in the northern Amazon, it peaks in March–April (TAB/TEF and

SAN) (Figure 5). The eastern Amazon (ALF and SAN) has a longer dry season than the western Amazon (TAB/TEF and RBA), although both areas receive a similar amount of annual rainfall [42].

On the other hand, the long dry season observed in ALF and SAN is governed by the South American Monsoon System, which is subject to oscillations due to the temperature of the tropical Atlantic ocean [43]. The interannual variability of the hydroclimatological system is strongly related to the El Niño/South Oscillation (ENSO). More generally, the sea surface temperature (SST) of the tropical Atlantic and Pacific control the variability of precipitation in the Amazon, and the anomalies of the southwest Atlantic SST influence the variability of the South Atlantic Convergence Zone (SACZ) centered at 10° S [44].

### 3.2. Contribution of Regions of Influence inside Amazonia

Analogous to the hydrological cycle, air masses carry gases and particles from one place to another, a process that varies by season. In the first and fourth quarters, during the rainy season, the most significant contribution of the region of influence occurs in the areas located to the north, in the region known as the Guiana Shield, in the Brazilian states of Amapá and Pará, and a small portion from the NE, from the Caatinga and Atlantic Forest biomes (Figure 6). The Amazonian region of influence ( $Amz\_perc$ , Equation (2)) for the combined period of the first and fourth quarters is 83% (sd = 8.3%) and 93% (sd = 3.3%) for the eastern and western Amazon, respectively (Figure 6).

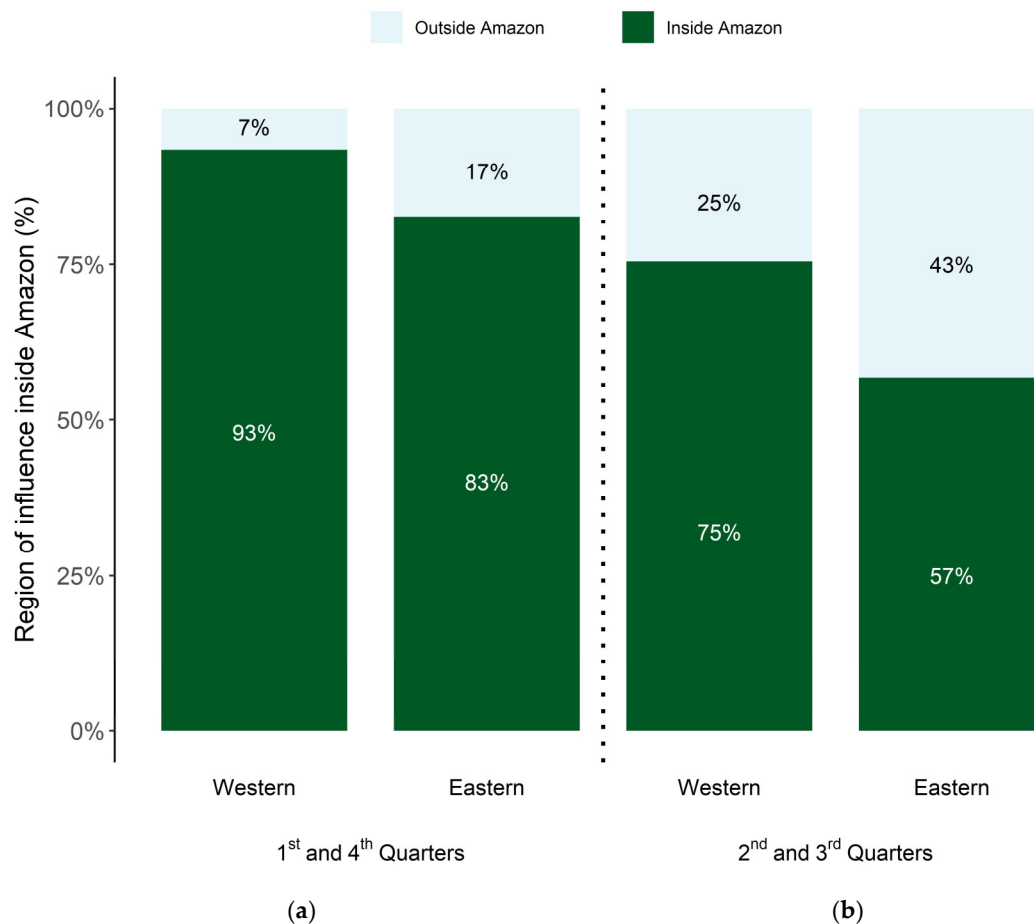


**Figure 6.** Nine-year average of the region of influence inside the Amazon biome ( $Amz\_perc$ ) by region for (a) first and fourth quarters, and (b) for second and third quarters. Eastern Amazon (SAN and ALF) and western Amazon (TAB/TEF and RBA).

During the second and third quarters, which culminate with the dry season, there is a higher percentage of the region of influence from continental areas outside the Amazon in the eastern

Amazon than in the western Amazon (Figure 6). The region of influence encompasses  $Amz\_perc = 57\%$  ( $sd = 8.8\%$ ) of the Amazon biome in the eastern Amazon and  $Amz\_perc = 75\%$  ( $6.5\%$ ) in the western Amazon during the second and third quarters (Figure 6).

There is also a high variability in the region of influence by quarter and site (Figure 7). For instance, the region of influence inside the Amazon at the ALF site is  $49\%$  ( $sd = 8.5\%$ ) during the second quarter (AMJ) (see Figure 5). On the other hand, TAB/TEF has the largest region of influence inside Amazon. During the first and fourth quarters (ONDJFM), all sites exhibit a region of influence inside the Amazon, on average, greater than  $80\%$  ( $sd = 5.2\%$ ). However, in the second and third quarters (AMJJAS), the region of influence inside the Amazon varies from  $49\%$  (ALF) to  $81\%$  (TAB/TEF) (Figure 7).

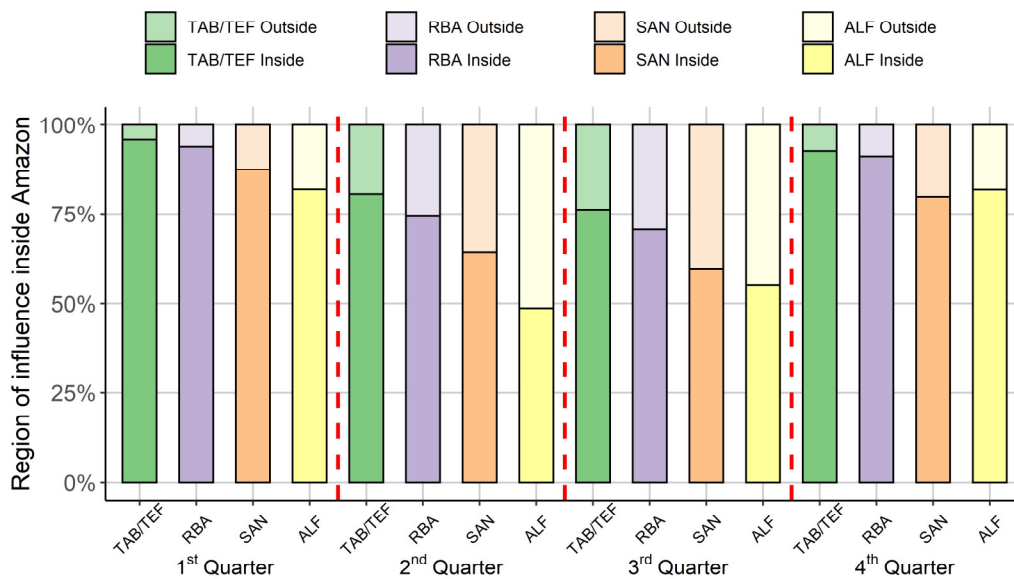


**Figure 7.** Percentage of weighted trajectories within the Amazon biome ( $Amz\_perc$ ) by quarter and site (nine-year averages).

Interannual variability is less pronounced than seasonal variability on the weighted region of influence in the Amazon, given by Equation (4) (Figure 8). During the drought years of 2010 and 2015/16, the weighted region of influence had the highest contribution on RBA  $weighted_{area} = 71\text{--}75\%$ , although it was not statistically different from other years ( $p > 0.99$ ). Due to the smallest extent of the region of influence and by being closest to the ocean where the trade winds are more consistent, the SAN site showed the lowest representativeness of the Amazon and interannual variability ( $weighted_{area} = 17\%$ ; Standard Error (SE) =  $3.8\%$ ). The interannual variability of the region of influence is also affected by anomalous exchanges of heating and cooling processes between sea surface temperature and atmosphere that occur at different time scales, such as the ENSO, which has a dominant frequency of oscillation every 3–4 years, on average; the Atlantic Multidecadal Oscillation (AMO), every 60–80 years; and Pacific Decadal Variability (PDV), every 1–20 years [42], which makes it difficult to predict its behavior.

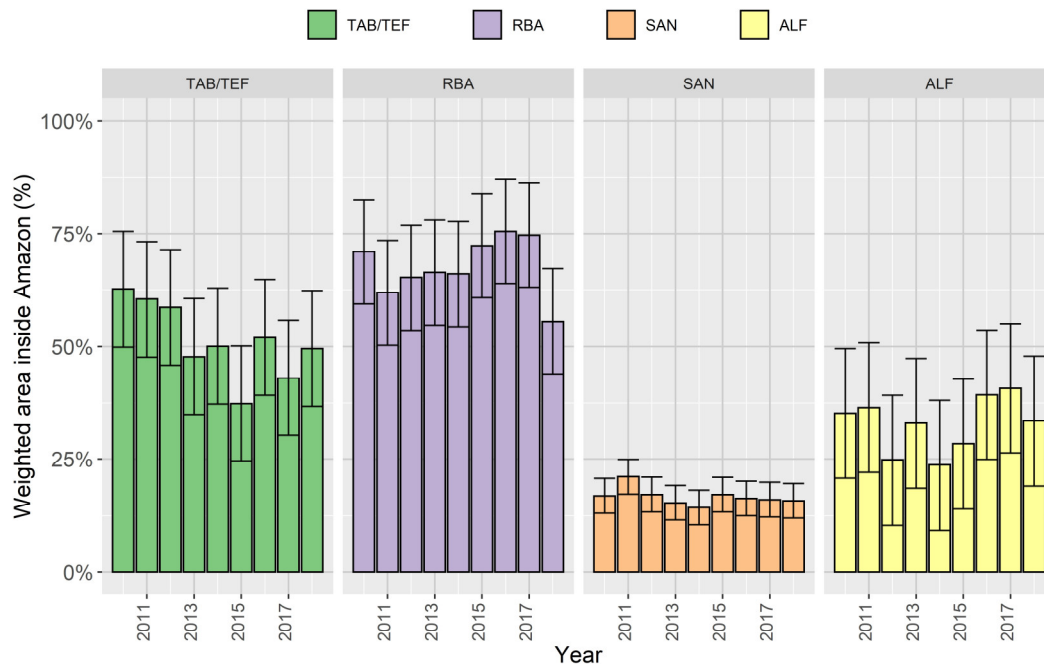


**Figure 8.** The representative area of each region of influence in the Amazon (7,256,362 km<sup>2</sup>) by site and year, following Equation (4). The error bar is the confidence interval from the mean and standard error (SE) at 95%.  $CI = \bar{x} \pm \frac{\sigma}{\sqrt{N}} Z_{95\%}$ .

### 3.3. Representativeness of the Region of Influence in the Amazon

Table 2 shows the western Amazon (RBA and TAB/TEF sites) is most representative, with 42–52.2% of the relative area inside the Amazon, respectively. In the eastern Amazon, it varies, on average, from 10.9% (SAN) to 25.3% (ALF). There are also seasonal and interannual differences in the representativeness of the region of influence. For instance, ALF has the highest intra-annual coefficient of variation of quarterly unweighted area ( $CV = 100 (\sigma/\bar{x}) = 58\%$ ) with a minimum area of 617,382 km<sup>2</sup> in the third quarter of 2012 and a maximum of 4,704,457 km<sup>2</sup> in the first quarter of 2018, whereas TAB/TEF and RBA have the lowest variation of the quarterly region of influence ( $CV = 24\%$ ) (Table 2). Additionally, SAN has a quarterly  $CV = 32\%$ . RBA has the greatest fraction of the Amazon among all the sites, including 79.8% of the Amazon in the fourth quarter of 2016. Furthermore, its smallest quarter still represents 26.0% of the Amazon in the third quarter of 2018 (Table 2). SAN is sensitive to the smallest fraction of Amazonia. On average, its highest proportion represents only 20.9% of the Amazon (first quarter of 2011) with a minimum of 7% in the fourth quarter of 2010 (Table 2).

Interannual variability is less pronounced than seasonal variability due to several reasons, such as air mass circulation patterns, displacement of the ITCZ by Atlantic SSTs, the influence of ENSO, and other variations [45,46]. ALF also has the highest interannual variability of unweighted area, with a minimum of 1,176,114 km<sup>2</sup> (2014: 16.2% of Amazon) and a maximum of 2,420,141 km<sup>2</sup> (2017: 33.4% of Amazon). RBA has the lowest interannual variation throughout the years ( $CV = 11\%$ ) followed by SAN ( $CV = 16\%$ ) and TAB/TEF ( $CV = 18\%$ ).

**Table 2.** Unweighted area of the region of influence in km<sup>2</sup> by quarter and year and its relative area in the Amazon biome (7,256,362 km<sup>2</sup>). Bold highlights the annual means of the region of influence at each site.

Year/ quarter	TAB/TEF		RBA		SAN		ALF	
	Area (km <sup>2</sup> )	Area (km <sup>2</sup> )	Area (km <sup>2</sup> )	% Amz	Area (km <sup>2</sup> )	% Amz	Area (km <sup>2</sup> )	% Amz
<b>2010</b>	<b>3,759,861</b>	<b>3,759,861</b>	<b>3,821,599</b>	<b>52.7%</b>	<b>645,165</b>	<b>8.9%</b>	<b>1,876,844</b>	<b>25.9%</b>
1st	4,753,849	4,753,849	4,309,332	59.4%	642,078	8.8%	2,111,450	29.1%
2nd	2,741,179	2,741,179	3,321,521	45.8%	617,383	8.5%	1,210,068	16.7%
3rd	4,136,467	4,136,467	3,333,864	45.9%	814,944	11.2%	1,197,722	16.5%
4th	3,407,951	3,407,951	4,321,678	59.6%	506,254	7.0%	2,988,134	41.2%
<b>2011</b>	<b>3,728,991</b>	<b>3,728,991</b>	<b>3,528,342</b>	<b>48.6%</b>	<b>1,083,506</b>	<b>14.9%</b>	<b>2,031,188</b>	<b>28.0%</b>
1st	3,815,425	3,815,425	4,358,723	60.1%	1,518,762	20.9%	3,593,166	49.5%
2nd	4,062,381	4,062,381	2,333,709	32.2%	679,120	9.4%	1,123,635	15.5%
3rd	3,728,989	3,728,989	3,099,259	42.7%	938,422	12.9%	950,770	13.1%
4th	3,309,170	3,309,170	4,321,677	59.6%	1,197,722	16.5%	2,457,182	33.9%
<b>2012</b>	<b>3,636,385</b>	<b>3,636,385</b>	<b>3,908,033</b>	<b>53.9%</b>	<b>814,945</b>	<b>11.2%</b>	<b>1,188,462</b>	<b>16.4%</b>
1st	3,568,471	3,568,471	4,185,853	57.7%	814,945	11.2%	1,654,587	22.8%
2nd	3,840,121	3,840,121	3,444,995	47.5%	617,382	8.5%	728,511	10.0%
3rd	3,432,648	3,432,648	3,444,997	47.5%	716,165	9.9%	617,382	8.5%
4th	3,704,297	3,704,297	4,556,285	62.8%	1,111,289	15.3%	1,753,367	24.2%
<b>2013</b>	<b>2,898,612</b>	<b>2,898,612</b>	<b>3,648,732</b>	<b>50.3%</b>	<b>830,379</b>	<b>11.4%</b>	<b>2,000,319</b>	<b>27.6%</b>
1st	1,926,235	1,926,235	4,556,283	62.8%	555,645	7.7%	3,074,565	42.4%
2nd	3,593,166	3,593,166	3,580,818	49.3%	629,730	8.7%	765,554	10.6%
3rd	3,296,825	3,296,825	2,271,968	31.3%	716,164	9.9%	1,148,331	15.8%
4th	2,778,223	2,778,223	4,185,857	57.7%	1,419,979	19.6%	3,012,827	41.5%
<b>2014</b>	<b>2,858,482</b>	<b>2,858,482</b>	<b>3,704,298</b>	<b>51.0%</b>	<b>691,468</b>	<b>9.5%</b>	<b>1,176,114</b>	<b>16.2%</b>
1st	2,062,059	2,062,059	3,827,774	52.8%	629,730	8.7%	1,666,932	23.0%
2nd	2,914,045	2,914,045	3,235,087	44.6%	753,206	10.4%	765,556	10.6%
3rd	2,531,270	2,531,270	2,975,787	41.0%	691,468	9.5%	938,422	12.9%
4th	3,926,554	3,926,554	4,778,544	65.9%	691,469	9.5%	1,333,547	18.4%
<b>2015</b>	<b>2,228,751</b>	<b>2,228,751</b>	<b>4,065,463</b>	<b>56.0%</b>	<b>839,640</b>	<b>11.6%</b>	<b>1,577,413</b>	<b>21.7%</b>
1st	2,531,269	2,531,269	4,420,460	60.9%	1,444,676	19.9%	2,901,700	40.0%
2nd	2,309,010	2,309,010	3,840,117	52.9%	642,078	8.8%	1,160,679	16.0%
3rd	1,827,453	1,827,453	3,370,906	46.5%	654,425	9.0%	1,222,417	16.8%
4th	2,247,272	2,247,272	4,630,368	63.8%	617,382	8.5%	1,024,856	14.1%
<b>2016</b>	<b>2,985,046</b>	<b>2,985,046</b>	<b>3,870,988</b>	<b>53.3%</b>	<b>743,946</b>	<b>10.3%</b>	<b>2,278,142</b>	<b>31.4%</b>
1st	2,259,621	2,259,621	3,938,900	54.3%	629,730	8.7%	2,951,091	40.7%
2nd	2,494,227	2,494,227	2,370,748	32.7%	802,599	11.1%	814,946	11.2%
3rd	3,012,828	3,012,828	3,383,256	46.6%	814,945	11.2%	1,815,103	25.0%
4th	4,173,507	4,173,507	5,791,048	79.8%	728,512	10.0%	3,531,428	48.7%
<b>2017</b>	<b>2,583,747</b>	<b>2,583,747</b>	<b>4,173,508</b>	<b>57.5%</b>	<b>731,598</b>	<b>10.1%</b>	<b>2,420,141</b>	<b>33.4%</b>
1st	2,247,273	2,247,273	4,753,848	65.5%	839,640	11.6%	4,704,457	64.8%
2nd	3,037,521	3,037,521	3,370,911	46.5%	765,554	10.6%	950,770	13.1%
3rd	2,617,704	2,617,704	2,901,697	40.0%	654,425	9.0%	1,024,856	14.1%
4th	2,432,489	2,432,489	5,667,574	78.1%	666,773	9.2%	3,000,482	41.3%
<b>2018</b>	<b>2,775,135</b>	<b>2,775,135</b>	<b>3,272,130</b>	<b>45.1%</b>	<b>722,338</b>	<b>10.0%</b>	<b>2,000,320</b>	<b>27.6%</b>
1st	2,531,268	2,531,268	3,815,424	52.6%	889,031	12.3%	3,667,254	50.5%
2nd	3,074,565	3,074,565	4,519,245	62.3%	790,249	10.9%	1,580,500	21.8%
3rd	3,111,606	3,111,606	1,889,192	26.0%	654,426	9.0%	913,727	12.6%
4th	2,383,098	2,383,098	2,864,657	39.5%	555,645	7.7%	1,839,801	25.4%
<b>Average</b>	<b>3,050,557</b>	<b>3,050,557</b>	<b>3,777,010</b>	<b>52.1%</b>	<b>789,221</b>	<b>10.9%</b>	<b>1,838,772</b>	<b>25.3%</b>

## 4. Discussion

### 4.1. What Is the Influence of Spatiotemporal Resolution on the Aggregation of the Results?

The region of influence is dependent on the trajectory density in each grid cell, as well as the extent of its area, which varies by site, quarter, and, somewhat less, by year. There is a trade-off between spatiotemporal aggregation and loss of temporal resolution. For instance, back-trajectories were binned quarterly but not by month or at each sample flask and altitude, as a typical “footprint” [21,36]. Lagrangian methods have an uncertainty of 15–30% to provide the correct location of the trajectory travel distance, meaning we only know a preferable distribution, not a specific place that an air parcel is coming from [47]. The underlying uncertainty of a particular region of influence is minimized on spatiotemporal aggregation by reducing the random errors from individual back-trajectories.

Time-span is another source of uncertainty in the region of influence method. Excluding one year of observational data, 2018, the average unweighted area decreases by only a maximum of 2%, regardless of the study site. This reduction in uncertainty is beneficial in cases where long-term average regions of influence are needed to determine the weighted average of upwind temporally static drivers, such as historical deforestation.

A more significant source of uncertainty of the Lagrangian model for a top-down estimate of GHG fluxes, however, is the planetary boundary layer (PBL) height, which has been estimated to result in 20% of estimated fluxes in an earlier study [48]. In Amazonia, the PBL height is relatively constant, reaching up to 1500 m asl, although vertical mixing of gases is influenced by deep moist convection—intense diurnal solar heating, shallow dry convection (i.e., shallow cumulus), and PBL height [49]. Indeed, the contribution of the trajectories at lower altitudes has a shorter range, meaning that they encompass a more significant weight inside Amazon, although this difference is relatively small (Figure 9A). Atmospheric aircraft vertical profiles sampling the column from 300 to 3500 m asl are sensitive to other GHG fluxes above the PBL, such as wildfire plumes. For instance, back-trajectories binned above the PBL (i.e., below 3500 m asl and above 1300 m asl) represent, on average, a region of influence 8% higher inside the Amazon than below its height (Figure 9B). On the other hand, the lower altitude reproduces a significant difference in the area covered by the region of influence due to the lowest number of back-trajectories computed, meaning that their relative area is condensed (less sparse) than up to 3500 m asl (Figure 9B). PBL heights HYSPLIT and GDAS will impact the regions of influence to some extent because they will influence the vertical profiles of wind speed and direction. However, the agreement between FLEXPART and HYSPLIT, which uses similar wind fields but different PBL schemes, suggests that the details of the PBL height may not be crucial for this method, which does not consider residence time of an air parcel in the PBL like a traditional footprint.

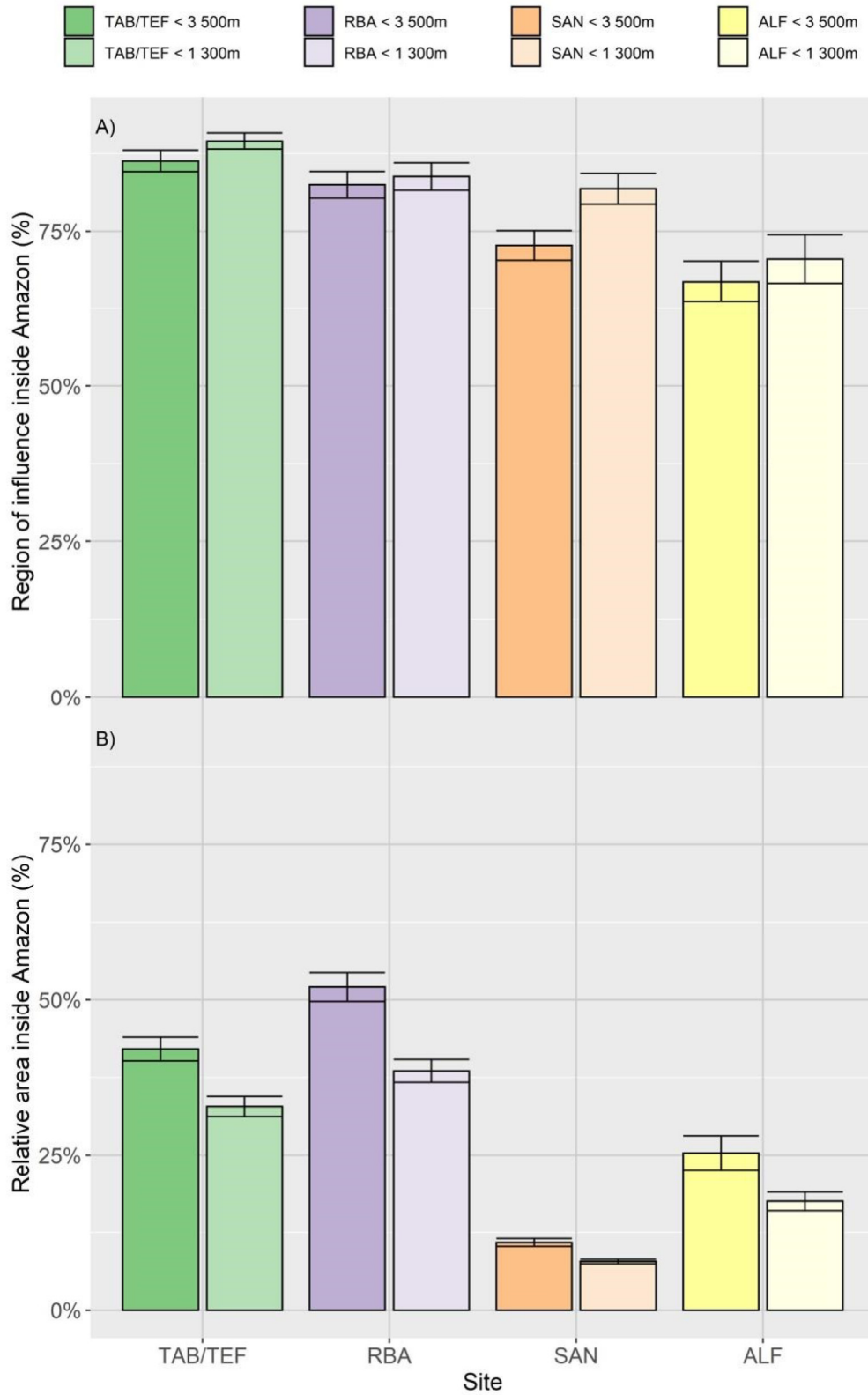


**Figure 9.** Difference between the ensemble back-trajectories up to planetary boundary layer (300–1300 m) and up to 3500 m at each study site. (A). Region of influence in the Amazon mask (Equation (2)) and (B). Relative area inside the Amazon (Equation (4)). Error bars are the standard error at a 95% significance level.

4.2. Limitations of the Method

As mentioned above, there are strong similarities between traditional “footprints” and our much simpler “regions of influence”. Using Equations (2) and (3), we compared the footprints used by Alden et al. [5] and our regions of influence for the years 2010–2012 for the same vertical profiles, although we recognize that both datasets do not have the same units. Figure S2 provides an example of comparisons between regions of influence and binned footprints, showing their similarity. To analyze the difference more thoroughly and quantitatively, footprints for each site, which were originally calculated for 12 or 17 levels per vertical profile, were totaled for the quarter, and rescaled to 1° spatial resolution (the original was 0.5°). We did not observe statistically significant differences in either  $Amz\_perc$  (Figure 10A, Equation (2)) or  $rel_{area}$  (Figure 10B, Equation (3)). This result gives us confidence that our simple back-trajectory density approach yields robust results for the relative spatial sensitivity of vertical profiles.

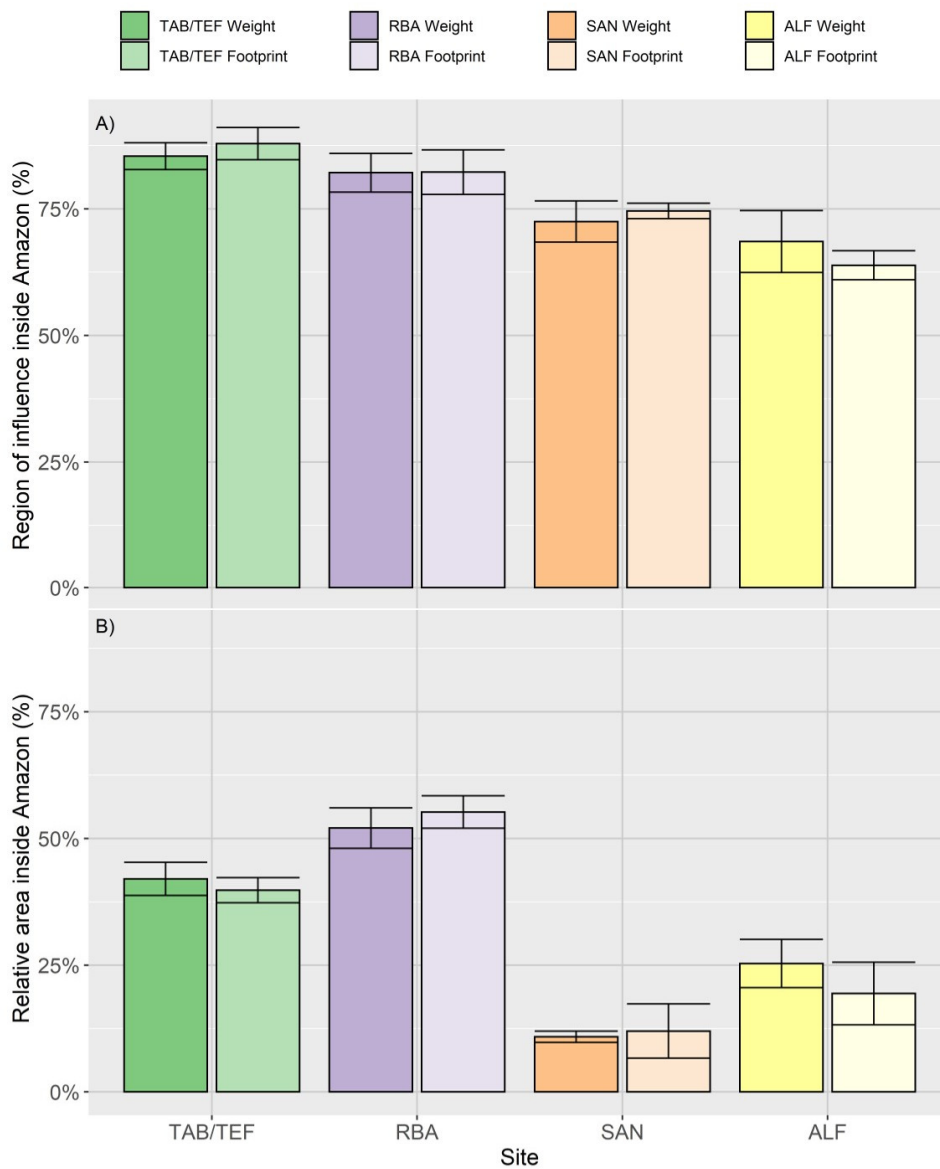


**Figure 10.** Difference between accumulated trajectories by footprint used by Alden [5] and the proposed method. (A) Region of influence inside the Amazon and (B) Relative area inside Amazon. Error bar is the standard error at a 95% significance level.

#### 4.3. What Are the Implications for Generalizations of GHG Fluxes at Regional Scales?

This study highlights the importance of defining the region of influence to understand the representativeness of Amazonian vertical profile air samples. Under our Amazon boundaries of more than seven million square kilometers, the regions of influence of the western sites are representative of almost 50% of the Amazon area. For eastern sites, the region of influence is less than 25% of the Amazon CARBAM mask (Table 2), so that extrapolation for the whole Amazon may result in inaccurate GHG fluxes. It has critical implications on representations of models across the Amazon, due to the mix of GHG flux contributions of savanna-dominated areas southward [36] and possibly a reason for differences in CO<sub>2</sub> source–sink estimation between bottom-up and top-down approaches [14,50].

## 5. Conclusions

Here, we present an approach to determine the region of influence of atmospheric aircraft vertical profiles to resolve the area of contribution spatially at regional scales in the Amazon using binned back-trajectories through a Lagrangian transport model. Using this method, we compute the region of influence and its representativeness (relative area) inside the Amazon at four distributed study sites in the Brazilian Amazon.

Air mass circulation patterns show significant seasonality by quarter, which is more pronounced than interannual variability. Large-scale forcing, primarily from the movement of the ITCZ, result in two main patterns: (a) the first and fourth quarters receive contributions from Northern Hemisphere air masses and the equatorial zone; and (b) the second and third quarters receive air masses exclusively with origins in the South Hemisphere. All quarters receive an important contribution from South American landmasses outside the Amazon (during the dry season), around 25–43%. The first and fourth quarters (wet season) show less influence from outside Amazonia (7–17%). Furthermore, due to the general atmospheric circulation and the proximity of the Atlantic coast, seasonal variability is more significant in the eastern Amazon (SAN and ALF sites) than in the western Amazon (RBA and TAB/TEF sites). The regions of influence in the western Amazon (TAB/TEF and RBA) represent, on average, 42–52% of the Amazon area, whereas in the eastern Amazon (SAN and ALF), they represent just 11–25% of the Amazon area, on average.

This research will support the ongoing objectives of the CARBAM project, which aims to resolve GHG fluxes in Amazonia for the Basin as a whole and spatially. The patterns of back-trajectories and the resultant regions of influence help us to understand the significant patterns of atmospheric circulation, providing insight into the connections between the measurements made at vertical profiling sites and the upwind land surface. In addition, the regions of influence can help define the average value of environmental drivers such as land use change, temperature, and precipitation that potentially contribute to GHG fluxes determined from vertical profile sites.

**Supplementary Materials:** The following are available online at [www.mdpi.com/2073-4433/11/10/1073/s1](http://www.mdpi.com/2073-4433/11/10/1073/s1), Table S1. Schedule flight plan by site and altitude. V2 and V3 are the system versions. Study sites are: SAN, RBA, ALF, and TAB/TEF. Figure S1. Distribution of the peak of fire plume in meters above sea level (m asl) at each study site. Figure S2. Comparison of the spatial distribution of the regions of influence provided by the density of trajectories from the method described in the text (left) and the surface sensitivity provided by FLEXPART footprints (right). Both datasets are on their original scales. In the main text Equations (1)–(3) were applied to both of them in order to compare them.

**Author Contributions:** Conceptualization, H.L.G.C., L.G.D., L.S.B. and L.V.G. and methodology, A.H.S.; L.G.D., H.L.G.C., L.V.G., L.S.B., and L.E.O.C.A.; software, L.D.G., A.H.S., E.A., L.S.B., L.M., J.B.M., C.C., and H.L.G.C.; validation, E.A., H.L.G.C. and C.B.A.; formal analysis, H.L.G.C.; investigation, H.L.G.C., L.G.D., L.S.B., L.V.G.; resources, L.V.G. and L.E.O.C.A.; data curation, H.L.G.C., L.G.D., L.S.B., L.V.G., G.P.T., and A.H.S.; writing—original draft preparation, H.L.G.C., L.S.B., G.P.T.; writing—review and editing L.O.A., L.V.G., L.G.D., M.G., J.B.M. and C.B.A.; visualization, H.L.G.C., L.S.B., G.P.T., L.V.G., and L.G.D.; supervision, L.V.G. and L.E.O.C.A.; project administration, L.V.G.; funding acquisition, L.V.G. All authors have read and agreed to the published version of the manuscript.

**Funding:** FAPESP: Grant No. 16/02018-2 funded this research. The H.L.G.C., L.S.B. and G.T.P. were funded by FAPESP Grant No. 2018/14423-4, 2018/14006-4, 2018/18493-7, respectively. L.O.A. thanks IAI (process: SGP-HW 016, CNPq process: 442650/2018- and 441949/2018-5).

**Acknowledgments:** We thank the NOAA Hysplit laboratory and the Large-scale Biosphere-Atmosphere program in Amazonia (LBA).

**Conflicts of Interest:** The authors declare no conflicts of interest.

## References

1. Ciais, P.; Sabine, C.; Bala, G.; Bopp, L.; Brovkin, V.; Canadell, J.; Chhabra, A.; DeFries, R.; Galloway, J.; Heimann, M.; et al. The physical science basis. Contribution of working group I to the fifth assessment report of the intergovernmental panel on climate change. *Chang. IPCC Clim.* **2013**, *1*, 465–570.
2. Friedlingstein, P.; Cox, P.; Betts, R.; Bopp, L.; von Bloh, W.; Brovkin, V.; Cadule, P.; Doney, S.; Eby, M.; Fung, I.; et al. Climate-carbon cycle feedback analysis: Results from the C4MIP model intercomparison. *J. Clim.* **2006**, *19*, 3337–3353.
3. Bloom, A.A.; Williams, M. Constraining ecosystem carbon dynamics in a data-limited world: Integrating ecological “common sense” in a model-data fusion framework. *Biogeosciences* **2015**, *12*, 1299–1315.
4. van der Laan-Luijkx, I.R.; Krol, M.C.; Gatti, L.V.; Domingues, L.G.; Correia, C.S.C.; Miller, J.B.; Gloor, M.; Leeuwen, T.T.; Kaiser, J.W.; Wiedinmyer, C.; et al. Global Biogeochemical Cycles drought derived with CarbonTracker South America. *Global Biogeochem. Cycles* **2015**, *29*, 1092–1108.
5. Alden, C.B.; Miller, J.B.; Gatti, L.V.; Gloor, M.M.; Guan, K.; Michalak, A.M.; van der Laan-Luijkx, I.T.; Touma, D.; Andrews, A.; Basso, L.S.; et al. Regional atmospheric CO<sub>2</sub> inversion reveals seasonal and geographic differences in Amazon net biome exchange. *Glob. Chang. Biol.* **2016**, *22*, 3427–3443.
6. Baldocchi, D.D.; Hincks, B.B.; Meyers, T.P. Measuring Biosphere-Atmosphere Exchanges of Biologically Related Gases with Micrometeorological Methods. *Ecology* **1988**, *69*, 1331–1340.
7. Knohl, A.; Baldocchi, D.D. Effects of diffuse radiation on canopy gas exchange processes in a forest ecosystem. *J. Geophys. Res. Biogeosci.* **2008**, *113*, doi:10.1029/2007JG000663.
8. Desjardins, R.L.; Worth, D.E.; Pattey, E.; VanderZaag, A.; Srinivasan, R.; Mauder, M.; Worthy, D.; Sweeney, C.; Metzger, S. The challenge of reconciling bottom-up agricultural methane emissions inventories with top-down measurements. *Agric. For. Meteorol.* **2018**, *248*, 48–59.
9. Gurney, K.R.; Law, R.M.; Denning, A.S.; Rayner, P.J.; Baker, D.; Bousquet, P.; Bruhwiler, L.; Chen, Y.-H.; Ciais, P.; Fan, S.; et al. Towards robust regional estimates of CO<sub>2</sub> sources and sinks using atmospheric transport models. *Nature* **2002**, *415*, 626–630.
10. Peters, W.; Jacobson, A.R.; Sweeney, C.; Andrews, A.E.; Conway, T.J.; Masarie, K.; Miller, J.B.; Bruhwiler, L.M.P.; Petron, G.; Hirsch, A.I.; et al. An atmospheric perspective on North American carbon dioxide exchange: CarbonTracker. *Proc. Natl. Acad. Sci. USA* **2007**, *104*, 18925–18930.
11. Jung, M.; Schwalm, C.; Migliavacca, M.; Walther, S.; Camps-Valls, G.; Koirala, S.; Anthoni, P.; Besnard, S.; Bodesheim, P.; Carvalhais, N.; et al. Scaling carbon fluxes from eddy covariance sites to globe: Synthesis and evaluation of the FLUXCOM approach. *Biogeosciences* **2020**, *17*, 1343–1365.
12. Gatti, L.V.; Gloor, M.; Miller, J.B.; Doughty, C.E.; Malhi, Y.; Domingues, L.G.; Basso, L.S.; Martinewski, A.; Correia, C.S.C.; Borges, V.F.; et al. Drought sensitivity of Amazonian carbon balance revealed by atmospheric measurements. *Nature* **2014**, *506*, 76–80.
13. Basso, L.S.; Gatti, L.V.; Gloor, M.; Miller, J.B.; Domingues, L.G.; Correia, C.S.C.; Borges, V.F. Seasonality and interannual variability of CH<sub>4</sub> fluxes from the eastern Amazon Basin inferred from atmospheric mole fraction profiles. *J. Geophys. Res. Atmos.* **2016**, *121*, 168–184.
14. Kondo, M.; Ichii, K.; Takagi, H.; Sasakawa, M. Comparison of the data-driven top-down and bottom-up global terrestrial CO<sub>2</sub> exchanges: GOSAT CO<sub>2</sub> inversion and empirical eddy flux upscaling. *J. Geophys. Res. Biogeosciences* **2015**, *120*, 1226–1245.
15. Basu, S.; Guerlet, S.; Butz, A.; Houweling, S.; Hasekamp, O.; Aben, I.; Krümmel, P.; Steele, P.; Langenfelds, R.; Torn, M.; et al. Global CO<sub>2</sub> fluxes estimated from GOSAT retrievals of total column CO<sub>2</sub>. *Atmos. Chem. Phys.* **2013**, *13*, 8695–8717.
16. Lin, J.C.; Gerbig, C.; Wofsy, S.C.; Andrews, A.E.; Daube, B.C.; Davis, K.J.; Grainger, C.A. A near-field tool for simulating the upstream influence of atmospheric observations: The Stochastic Time-Inverted Lagrangian Transport (STILT) model. *J. Geophys. Res. Atmos.* **2003**, *108*, doi:10.1029/2002JD003161.

17. Stohl, A.; Hittenberger, M.; Wotawa, G. Validation of the Lagrangian particle dispersion model FLEXPART against large-scale tracer experiment data. *Atmos. Environ.* **1998**, *32*, 4245–4264.
18. Gerbig, C.; Lin, J.C.; Wofsy, S.C.; Daube, B.C.; Andrews, A.E.; Stephens, B.B.; Bakwin, P.S.; Grainger, C.A. Toward constraining regional-scale fluxes of CO<sub>2</sub> with atmospheric observations over a continent: 2. Analysis of COBRA data using a receptor-oriented framework. *J. Geophys. Res. Atmos.* **2003**, *108*, doi:10.1029/2003JD003770.
19. Hu, L.; Andrews, A.E.; Thoning, K.W.; Sweeney, C.; Miller, J.B.; Michalak, A.M.; Dlugokencky, E.; Tans, P.P.; Shiga, Y.P.; Mountain, M.; et al. Enhanced North American carbon uptake associated with El Niño. *Sci. Adv.* **2019**, *5*, 1–11.
20. Martins, D.K.; Sweeney, C.; Stirm, B.H.; Shepson, P.B. Regional surface flux of CO<sub>2</sub> inferred from changes in the advected CO<sub>2</sub> column density. *Agric. For. Meteorol.* **2009**, *149*, 1674–1685.
21. Draxler, R.R.; Hess, G.D. An overview of the HYSPLIT\_4 modelling system for trajectories, dispersion and deposition. *Aust. Meteorol. Mag.* **1998**, *47*, 295–308.
22. Eva, H.D.; Huber, O.; Achard, F.; Balslev, H.; Beck, S.; Behling, H.; Belward, A.S.; Beuchle, R.; Cleef, A.M.; Colchester, M.; et al. *A Proposal for Defining the Geographical Boundaries of Amazonia; Synthesis of the Results from an Expert Consultation Workshop Organized by the European Commission in Collaboration with the Amazon Cooperation Treaty Organization—JRC Ispra, 7–8 June 2005*; EC: Luxembourg, 2005; ISBN 9279000128.
23. Olson, D.M.; Dinerstein, E.; Wikramanayake, E.D.; Burgess, N.D.; Powell, G.V.N.; Underwood, E.C.; D’Amico, J.A.; Itoua, I.; Strand, H.E.; Morrison, J.C.; et al. Terrestrial Ecoregions of the World: A New Map of Life on Earth. *Bioscience* **2001**, *51*, 933.
24. FAPESP—São Paulo Research Foundation. CARBAM Project: The Amazon Carbon Balance Long-Term Study. Available online: <https://bv.fapesp.br/en/auxilios/97938/interannual-variation-of-amazon-basin-greenhouse-gas-balances-and-their-controls-in-a-warming-and-in/> (accessed on 18 June 2020).
25. Gatti, L.V.; Miller, J.B.; D’Amelio, M.T. aS.; Martinewski, A.; Basso, L.S.; Gloor, M.E.; Wofsy, S.; Tans, P. Vertical profiles of CO<sub>2</sub> above eastern Amazonia suggest a net carbon flux to the atmosphere and balanced biosphere between 2000 and 2009. *Tellus B Chem. Phys. Meteorol.* **2010**, *62*, 581–594.
26. Coe, M.T.; Macedo, M.N.; Brando, P.M.; Lefebvre, P.; Panday, P.; Silvério, D. The Hydrology and Energy Balance of the Amazon Basin. In *Ecological Studies*; Nagy, L., Forsberg, B.R., Artaxo, P., Eds.; Ecological Studies; Springer Berlin Heidelberg: Berlin/Heidelberg, Germany, 2016; Volume 227, pp. 139–148. ISBN 978-3-662-49900-9.
27. Climate Data. Climate Model with 220 mi Points Interpolated in 30 Arc Seconds Spatial Resolution. Data from 1982 to 2012. Available online: <https://pt.climate-data.org/> (accessed on 17 May 2020).
28. INPE. Amazon Deforestation Monitoring Project (PRODES). São José dos Campos, SP, Brazil, 2019. Available online: <http://www.obt.inpe.br/OBT/assuntos/programas/amazonia/prodes> (accessed on 18 May 2020).
29. Tejada, G.; Dalla-Nora, E.; Cordoba, D.; Laforteza, R.; Ovando, A.; Assis, T.; Aguiar, A.P. Deforestation scenarios for the Bolivian lowlands. *Environ. Res.* **2016**, *144*, 49–63.
30. Ometto, J.P.; Sousa-Neto, E.R.; Tejada, G. Land Use, Land Cover and Land Use Change in the Brazilian Amazon (1960–2013). In *Ecological Studies*; Springer: Berlin, Germany, 2016; Volume 227, pp. 369–383. ISBN 978-3-662-49900-9.
31. Mapbiomas. Proyecto MapBiomas Amazonía—Colección [1.0] de los mapas anuales de cobertura y uso del suelo. Available online: <http://amazonia.mapbiomas.org> (accessed on 18 April 2019).
32. Miller, J.B.; Gatti, L.V.; D’Amelio, M.T.S.; Crotwell, A.M.; Dlugokencky, E.J.; Bakwin, P.; Artaxo, P.; Tans, P.P. Airborne measurements indicate large methane emissions from the eastern Amazon basin. *Geophys. Res. Lett.* **2007**, *34*, L10809.
33. Domingues, L.G. As emissões de carbono provenientes da queima de biomassa e os fatores que a influenciam na Amazônia, 2019. Ph.D. Thesis, Ciências na Área de Tecnologia Nuclear, Instituto de Pesquisas Energéticas e Nucleares, Universidade de São Paulo, São Paulo, Brazil, 23 September 2019.
34. Stein, A.F.; Draxler, R.R.; Rolph, G.D.; Stunder, B.J.B.; Cohen, M.D.; Ngan, F. NOAA’s HYSPLIT Atmospheric Transport and Dispersion Modeling System. *Bull. Am. Meteorol. Soc.* **2015**, *96*, 2059–2077.
35. Draxler, R.R.; Rolph, G.D. Evaluation of the Transfer Coefficient Matrix (TCM) approach to model the atmospheric radionuclide air concentrations from Fukushima. *J. Geophys. Res. Atmos.* **2012**, *117*, doi:10.1029/2011JD017205.

36. Pöhlker, C.; Walter, D.; Paulsen, H.; Könemann, T.; Rodríguez-Caballero, E.; Moran-Zuloaga, D.; Brito, J.; Carbone, S.; Degrendele, C.; Després, V.R.; et al. Land cover and its transformation in the backward trajectory footprint region of the Amazon Tall Tower Observatory. *Atmos. Chem. Phys.* **2019**, *19*, 8425–8470.
37. Rolph, G.; Stein, A.; Stunder, B. Real-time Environmental Applications and Display sYstem: READY. *Environ. Model. Softw.* **2017**, *95*, 210–228.
38. Gatti Domingues, L.; Vanni Gatti, L.; Aquino, A.; Sánchez, A.; Correia, C.; Gloor, M.; Peters, W.; Miller, J.; Turnbull, J.; Santana, R.; et al. A New Background Method for Greenhouse Gases Flux Calculation Based in Back-Trajectories Over the Amazon. *Atmosphere (Basel)* **2020**, *11*, 734.
39. R Development Core Team. *R: A Language and Environment for Statistical Computing*; R Development Core Team: Vienna, Austria, 2008.
40. Cavalcanti, I.F.A.; Ferreira, N.J.; Dias, M.A.F.S.; Silva, M.G.A.J. *Tempo e clima no Brasil*, 1st ed.; Editora Oficina de Textos: Rio de Janeiro, Brasil, 2009; 454p.
41. Marengo, J.A.; Souza, C.M.; Thonicke, K.; Burton, C.; Halladay, K.; Betts, R.A.; Alves, L.M.; Soares, W.R. Changes in Climate and Land Use Over the Amazon Region: Current and Future Variability and Trends. *Front. Earth Sci.* **2018**, *6*, 228.
42. Figueroa, Silvio, N.; Nobre, C.A. Precipitation distribution over central and western tropical South America. *Climanálise* **1990**, *5*, 36–45.
43. Fu, R.; Arias, P.A.; Wang, H. The Connection between the North and South American Monsoons. *Springer Clim.* **2016**, 187–206.
44. Nobre, C.A.; Obregón, G.O.; Marengo, J.A. Características do Clima Amazônico: Aspectos Principais. *Amaz. Glob. Chang.* **2009**, 149–162.
45. Marengo, J.A. Interannual variability of deep convection over the tropical South American sector as deduced from ISCCP C2 data. *Int. J. Climatol.* **1995**, *15*, 995–1010.
46. Salati, E.; Marques, J. Climatology of the Amazon region. In *The Amazon—Limnology and Landscape Ecology of a Mighty Tropical River and Its Basin*; Sioli, H., Ed.; Dr. W. Junk Publishers: Devon, UK, 1984; pp. 85–126.
47. NOAA—National Oceanic and Atmospheric Administration. ASL—Air Resources Laboratory. Hysplit. Available online: <https://www.arl.noaa.gov/hysplit/hysplit-frequently-asked-questions-faqs/faq-hg11/> (accessed on 18 June 2020).
48. Brioude, J.; Angevine, W.M.; McKeen, S.A.; Hsie, E.-Y. Numerical uncertainty at mesoscale in a Lagrangian model in complex terrain. *Geosci. Model Dev.* **2012**, *5*, 1127–1136.
49. Oliveira, M.I.; Acevedo, O.C.; Sörgel, M.; Nascimento, E.L.; Manzi, A.O.; Oliveira, P.E.S.; Brondani, D.V.; Tsokankunku, A.; Andreae, M.O. Planetary boundary layer evolution over the Amazon rainforest in episodes of deep moist convection at the Amazon Tall Tower Observatory. *Atmos. Chem. Phys.* **2020**, *20*, 15–27.
50. Van der Laan-Luijkx, I.T.; van der Velde, I.R.; Krol, M.C.; Gatti, L.V.; Domingues, L.G.; Correia, C.S.C.; Miller, J.B.; Gloor, M.; van Leeuwen, T.T.; Kaiser, J.W.; et al. Response of the Amazon carbon balance to the 2010 drought derived with CarbonTracker South America. *Global. Biogeochem. Cycles* **2015**, *29*, 1092–1108.

